

UNIVERSIDADE FEDERAL DE ITAJUBÁ - UNIFEI  
POSTGRADUATE PROGRAM IN  
PHYSICS

Development of an Automated Apparatus  
for Spray Coating and the Influence of  
Calcination Temperature on Titanium  
Dioxide Photocatalytic Activity.

João H.B. Pinton

Itajubá, 8 de novembro de 2024

UNIVERSIDADE FEDERAL DE ITAJUBÁ - UNIFEI  
POSTGRADUATE PROGRAM IN  
PHYSICS

João H.B. Pinton

Development of an Automated Apparatus  
for Spray Coating and the Influence of  
Calcination Temperature on Titanium  
Dioxide Photocatalytic Activity.

Dissertation submitted to the Graduate Program in Physics  
as part of the requirements for obtaining the degree of Master  
of Science in Physics.

**Concentration Area: Experimental Condensed Mat-  
ter Physics**

**Orientador: Prof. Dr. Adhimar Flávio Oliveira**

**Coorientador: Prof. Dr. Danilo Roque Huanca**

**8 de novembro de 2024**

**Itajubá**

UNIVERSIDADE FEDERAL DE ITAJUBÁ - UNIFEI  
POSTGRADUATE PROGRAM IN  
PHYSICS

Development of an Automated Apparatus  
for Spray Coating and the Influence of  
Calcination Temperature on Titanium  
Dioxide Photocatalytic Activity.

João H.B. Pinton

Dissertation approved by the examination committee on 8 of November of 2024, conferring upon the author the title of **Master of Science in Physics**

*Banca Examinadora:*

Prof. Dr. Nelcy D.S Mohallem

Prof. Dr. Suelen de Castro

Itajubá

2024

---

João H.B. Pinton

Development of an Automated Apparatus for Spray Coating and the Influence of Calcination Temperature on Titanium Dioxide Photocatalytic Activity/ João H.B. Pinton. – Itajubá, 12 de novembro de 2024-

54 p.

Orientador: Prof. Dr. Adhimar Flávio Oliveira

Dissertação (Mestrado)

Universidade Federal de Itajubá - UNIFEI

Postgraduate Program in Physics, 8 de novembro de 2024.

1. Photocatalysis. 2. Spray coating.

---

João H.B. Pinton

**Development of an Automated Apparatus for Spray  
Coating and the Influence of Calcination  
Temperature on Titanium Dioxide Photocatalytic  
Activity**

Dissertation submitted to the Graduate  
Program in Physics as part of the requi-  
rements for obtaining the degree of Mas-  
ter of Science in Physics.

Trabalho aprovado. Itajubá, 8 de Novembro de 2024:

---

**Prof. Dr. Adhimar Flávio Oliveira**  
Orientador

---

**Prof. Dr. Danilo Roque Huanca**  
Coorientador

---

**Prof. Dr. Nelcy D.S Mohallem**

---

**Prof. Dr. Suelen de Castro**

Itajubá  
8 de novembro de 2024

# 1 Acknowledgments

The authors would like to thank the Brazilian agency CAPES and Fapemig (Finance Code APQ-00010-18) for their financial support.

*"If I have seen further it is by standing on the shoulders of Giants."  
(Isaac Newton)*

## Abstract

This work presents the development of a low-cost device for automated sol-gel solution deposition, using spray coating technique for the synthesis of TiO<sub>2</sub> thin films. The as-obtained films were submitted to different thermal treatment with the purpose of investigating the respective impacts on photocatalytic efficiency. The films were characterized through the use of X-Ray Diffraction (XRD), Scanning electron microscope (SEM), Atomic Force Microscopy (AFM), Fourier-Transform Infrared Spectroscopy (FTIR), and UV-Vis spectroscopy. Later, it was indeed confirmed that the anatase phase predominates in the temperature range considered in this research. Better crystallization and larger crystallite size were obtained with the increase of the temperature, leading to a larger surface roughness, consequently exhibiting a good impact on photocatalytic activities and degradation efficiency. Notably, the films calcined at 600 °C exhibited the highest efficiency, achieving near-complete degradation of methylene blue within 4 hours under UV light. This work emphasizes the effectiveness of the developed spray coating device in fabricating high-quality TiO<sub>2</sub> films and demonstrates the importance of thermal treatment temperature in improving photocatalytic degradation, contributing to practical applications for sustainable water treatment.

**Key-words:** Sol-gel, Spray coating, TiO<sub>2</sub> films, Sustainable solutions.

# List of Figures

Figure 1 – Photon-semiconductor interaction responsible for the formation of electron-hole pairs, the process responsible for the formation of degrading agents. . . . .	16
Figure 2 – (a) Glass substrate where the sol-gel solution is deposited. (b) A spray nozzle that disperses the coating fluid. (c) The Stepper motor was controlled by Arduino, where parameters such as speed, time between depositions, and amplitude of movement were controlled. . . . .	20
Figure 3 – Drying process representation in which the substrate with the coating fluid was subjected to obtain the TiO <sub>2</sub> thin film. . . . .	21
Figure 4 – Thermogravimetric analysis (TGA) of the coating fluid. . . . .	24
Figure 5 – (a) Reference curves obtained through controlled dilution of the initial methylene blue solution. (b) Linear fit for concentration determination, enabling the determination of these values from absorbance measurements. . . . .	25
Figure 6 – The emission spectrum of the 15W lamp used for the photocatalysis procedure. . . . .	25
Figure 7 – (a) TiO <sub>2</sub> powder created through the identical calcination process as the thin film, employing the coating liquid. (b) Titanium mapping was conducted via Energy-dispersive X-ray spectroscopy. (c) Oxygen mapping was conducted via Energy-dispersive X-ray spectroscopy. (d) Titanium/oxygen concentration ratio in the thin film. . . . .	28
Figure 8 – (a) Image showing the fragmentation of the thin film where the thickness measurement was conducted. (b) Adjustment through a normal distribution, from which the value of the average film thickness along with its corresponding standard deviation was obtained. . . . .	29

Figure 9 – Fourier-transform infrared spectroscopy spectra of: (a) TiO <sub>2</sub> thin film and (b) TiO <sub>2</sub> powder. . . . .	30
Figure 10 – UV-Vis Absorption Spectra: A comparison of absorbance spectra between the thin film (a) and powder diluted in distilled water (b). The changes in peak positions provide information about the optical properties. . . . .	31
Figure 11 – (a) TiO <sub>2</sub> Nanopowder (b) TiO <sub>2</sub> Thin film and (c) Pattern JCPDS 01-084-1285 anatase TiO <sub>2</sub> . In (b) it is possible to observe the presence of peaks corresponding to the anatase structural pattern, as well as an amorphous region due to the presence of the glass substrate. . . . .	32
Figure 12 – Degradation process of methyl blue (a) and methyl orange (b) as a function of ultraviolet light exposure time. . . . .	33
Figure 13 – Visual degradation process of methyl blue (a) and methyl orange (b). . . . .	33
Figure 14 – (a) Efficiency of photodegradation of MB and MO with ultraviolet light irradiation on TiO <sub>2</sub> films, where curve (I) represents photocatalysis and (II) Autodegradation of MB. (b) Kinetic data for the degradation of MB and MO. . . . .	35
Figure 15 – Contact angle measurement evaluating the surface wettability of the TiO <sub>2</sub> thin film in contact with water. . . . .	36
Figure 16 – Diffractogram for different calcination temperatures of TiO <sub>2</sub> thin films. . . . .	37
Figure 17 – AFM micrograph (2D) of the TiO <sub>2</sub> thin films with different calcination temperature, (a) 300 °C, (b) 400 °C, (c) 500 °C and (d) 600 °C. . . . .	39
Figure 18 – AFM micrograph (3D) of the TiO <sub>2</sub> thin films with different calcination temperature, (a) 300 °C, (b) 400 °C, (c) 500 °C and (d) 600 °C. . . . .	40
Figure 19 – The spectra obtained by FTIR analysis (a) show the characteristic absorption bands of the starting materials, while (b) highlights the formation of TiO <sub>2</sub> , despite the spectral range limitation. . . . .	41

Figure 20 – Absorbance curves of the MB solution after the photocatalysis process using reactors calcined at different temperatures: (a) 300 °C, (b) 400 °C, (c) 500 °C, and (d) 600 °C. . . . .	42
Figure 21 – Degradation efficiency (DE) obtained for reactors at different temperatures. . . . .	43
Figure 22 – Pseudo first-order rate constant (k) obtained for reactors at different temperatures. . . . .	44
Figure 23 – Stability test of the photocatalyst over 10 degradation cycles. . .	46

# List of Tables

Table 1 – Effects of Calcination Temperature on Thin Film Properties . . .	38
Table 2 – Values of the reaction kinetics for reactors calcined at different temperatures. . . . .	45

# Contents

1	<b>ACKNOWLEDGMENTS</b> . . . . .	7
2	<b>INTRODUCTION</b> . . . . .	15
2.1	<b>Photocatalysis Mechanism</b> . . . . .	16
3	<b>EXPERIMENTAL METODOLOGY</b> . . . . .	18
3.1	<b>Spray-Coating Solution</b> . . . . .	18
3.2	<b>First Research</b> . . . . .	18
3.3	<b>Second Research</b> . . . . .	22
4	<b>RESULTS</b> . . . . .	27
4.1	<b>First Research</b> . . . . .	27
4.2	<b>Second Research</b> . . . . .	36
5	<b>CONCLUSION</b> . . . . .	48
	<b>BIBLIOGRAPHY</b> . . . . .	49

## 2 Introduction

In today's world, there is a growing concern regarding environmental pollution, energy scarcity, and fuel production [1]. Titanium dioxide ( $\text{TiO}_2$ ) emerges as a highly promising material due to its non-toxicity, biological compatibility, and cost-effectiveness [2]. Notably this semiconductor demonstrates remarkable versatility, finding applications in the areas mentioned earlier [3, 4, 5].

This versatility is primarily attributed to  $\text{TiO}_2$  thin films and their exceptional ability to photocatalysis [6, 7]. Through the absorption of ultraviolet solar radiation,  $\text{TiO}_2$  generates electron-hole pairs, which can be effectively harnessed for electron transfer (redox) processes [8], whose charge carriers react with chemical species [9, 10]. Consequently, this process enables both pollution degradation [11], bactericidal effect [12] and production of clean energy [13]. Photocatalysis is a significant tool in the degradation of contaminants of emerging concern (CECs), which have garnered attention due to their adverse effects on human health and the environment [14, 15]. These pollutants encompass dyes [16], contraceptives [17], antibiotics [18], and various pharmaceuticals.

In the context of synthesis, various techniques, such as atomic layer deposition (ALD) [19], spray pyrolysis [20], and spray coating [21], have been utilized for the fabrication of thin films, nanoparticles, nanocomposites, nanotubes, and other nanostructures [22, 23, 24, 25]. Thin films in photocatalysis offer significant advantages compared to powder usage. They enable precise control over the morphology and structure of the catalytic surface, resulting in enhanced efficiency and improved mass and energy transfer [26]. Additionally, they eliminate the need for catalyst separation and recovery post-reaction, facilitating reusability without material loss. Thin films prevent particle aggregation, can be applied to a variety of substrates, and exhibit greater mechanical stability and resistance to degradation, thereby reducing the risk of final product contamination [27, 28, 29].

The spray-coating method proves to be cost-effective and efficient, thus emphasizing in this research the development of a device for the deposition of

sol-gel solutions using the spray-coating technique, this made possible to investigate the utilization of TiO<sub>2</sub> thin films, assessing the effects of different calcination temperatures on morphology, composition, degradation efficiency (DE), and degradation kinetics (k), using the methylene blue as a degradation target. We also explored the stability and reusability of the films over 15 photocatalytic cycles. These findings contribute to the development of more effective devices for pollutant degradation in the environment.

## 2.1 Photocatalysis Mechanism

Photocatalysis is derived from the fact that photons with sufficient energy, when incident on a semiconductor, can promote electrons from the valence band to the conduction band, as illustrated in Fig. 1.

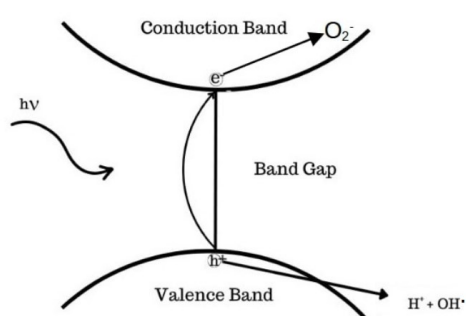


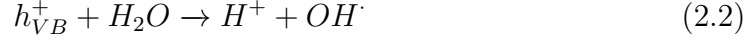
Figure 1 – Photon-semiconductor interaction responsible for the formation of electron-hole pairs, the process responsible for the formation of degrading agents.

This behavior is responsible for the creation of electron-hole pairs, as represented in Equation 2.1.



With the creation of pairs, it is necessary for the material to satisfactorily promote photocatalysis, that the redox potential of the photogenerated hole in the valence

band (VB) ( $h_{VB}^+$ ) be sufficiently positive to generate the formation of hydroxyl radicals ( $OH\cdot$ ), as shown in Eq.2.2. This is a highly reactive chemical species that will oxidize the organics [30].



On the other hand, the photogenerated electron in the conduction band (CB) ( $e_{CB}^-$ ) must have a sufficiently negative potential for the formation of superoxide radical anions ( $O_2^-$ ), as represented in Eq.2.3. The formation of these superoxides is also important because their formation prevents the recombination of electron-hole pairs [31].



It is worth noting that the electron-hole pairs that recombine, as shown in Equation 2.4, do not contribute to the performance of photocatalysis.



Finally, the photocatalysis mechanism relies on the interaction between photons and semiconductors, leading to the creation of electron-hole pairs. This phenomenon, illustrated in Figure 1, initiates the pollutant degradation process. The photogenerated holes in the valence band ( $h_{VB}^+$ ) oxidize water molecules to form hydroxyl radicals ( $OH\cdot$ ), while the photogenerated electrons in the conduction band ( $e_{CB}^-$ ) react with oxygen to produce superoxide radical anions ( $O_2^-$ ). These radicals play crucial roles in oxidizing organic pollutants and preventing the recombination of electron-hole pairs, thereby enhancing the efficiency of photocatalysis. Minimizing the recombination of electron-hole pairs, as illustrated in Equation 2.4, is imperative as this process diminishes the effectiveness of the photocatalytic reaction. Understanding these mechanisms is essential for defining and optimizing photocatalytic materials for various environmental remediation applications.

## 3 Experimental Methodology

### 3.1 Spray-Coating Solution

For the preparation of the solution under study, Xylene from the Lab-Synth laboratory, Titanium (IV) butoxide (98% purity) and Triton X-100 from the Sigma-Aldrich laboratory, along with distilled water, were used. The preparation process involved adding 0.026 moles of Xylene to  $6.60 \times 10^{-3}$  moles of Triton X-100. This mixture was stirred using a magnetic stirrer at 1000 rpm for 30 minutes at room temperature (25°C). Subsequently,  $1.47 \times 10^{-2}$  moles of titanium (IV) butoxide and 0.3 ml of distilled water were added. The stirring process was then continued for an additional 5 hours, ensuring complete homogeneity of the coating fluid solution.

### 3.2 First Research

The glass substrates were subjected to a meticulous cleaning procedure utilizing an ultrasonic apparatus. Initially, the glass substrates were immersed in a solution composed of distilled water, along with alkaline agents, mildly abrasive components and ionic surfactants, for 1 hour. The objective was to eliminate organic impurities. Subsequently, this solution was discarded, and the substrates underwent an ultrasonic cleansing procedure using only distilled water, aiming to remove any traces of the previous solution from their surfaces. Afterward, the procedure was reiterated using acetone and isopropyl alcohol, with each solvent undergoing a 1-hour ultrasonic immersion, to remove hydrocarbons and weakly polar organics [32]. The process concluded with the substrates being dried using a flow of dry compressed air.

With the completion of the preceding stages, the next step involved depositing the coating fluid onto the clean substrates. The device in question allows parameter adjustments aimed at enhancing film quality and uniformity. It was ob-

served that upon activating the compressor, it took approximately 0.5 seconds for the spray to achieve uniformity. Consequently, this information had to be taken into account when determining the values for the amplitude of movement and the activation and deactivation timing of the compressor. This was attempted to reduce the thickness difference between the center and the edges of the film, aiming for the film to exhibit the most uniform thickness possible.

Other factors, such as the base's displacement speed and the solution flow through the spray nozzle, were also fine-tuned to prevent the synthesis of excessively thick films. The distance between the spray nozzle and the substrate for these films was set at 10 cm. This distance can be adjusted according to future deposition requirements. In this research, the synthesized films consist of a single layer only, eliminating the need to define a time interval between depositions.

After the completion of the coating fluid deposition, the sample was allowed to dry at room temperature (25°C) for 6 hours. Following this, the sample underwent a 24-hour thermal treatment at a temperature of 60°C, with a temperature gradient of 1°C per minute. This gradient was established to minimize and even prevent the formation of cracks in the film. After that, it underwent another thermal treatment carried out to eliminate volatile compounds, a process known as calcination shown in Figure 3. Thermal Gravimetric Analysis (TGA) was used to characterize the thermal behavior of TiO<sub>2</sub> from its main thermal degradation temperatures from the respective mass losses. The equipment used was a Shimadzu TGA-50. For the TGA analysis, a mass of approximately 5 mg per sample was used, in the temperature range of 25-1000°C with a flow rate of 10°C/min, in a nitrogen atmosphere with a flow of 30 mL/min, based on this analysis, a temperature of 400°C was determined as the optimal choice for the sample's calcination process, as shown in Figure 4. The sample was maintained in this condition for an additional 24 hours, employing the same gradient as before. The cooling process was carried out with the oven remaining closed, avoiding sudden temperature changes that might lead to cracking or compromise the film's quality.

The sample characterizations were conducted using a Scanning Electron Microscope (SEM) and Energy-dispersive X-ray Spectroscopy (EDS) utilizing the Carls Zeiss EVO MA 15 model. X-ray Diffraction (XRD) was also employed, using

the equipment from PANalytical model X'Pert PRO, which emits Cu-K $\alpha$  radiation. The XRD parameters included a scan range of  $2\theta$  from  $20^\circ$  to  $80^\circ$ , a step size of  $0.02^\circ$ , and a time per step of 2 seconds. Additionally, Ultraviolet–Visible spectroscopy (UV-Vis) was performed, with measurements taken from 600 nm to 250 nm and a step interval of 0.5 nm. The solution used for deposition underwent a thermal treatment at  $400^\circ\text{C}$  with a gradient of  $1^\circ\text{C}/\text{min}$ . Upon reaching the desired temperature, the solution was held under these conditions for 12 hours, resulting in an anatase TiO<sub>2</sub> powder. This anatase powder was diluted in distilled water, and its absorbance was measured using a quartz cuvette. To ensure that the measured absorbance was solely attributed to the TiO<sub>2</sub> powder, the reference used for the measurement was a quartz cuvette filled with distilled water. Additionally, the measurement of the thin film was conducted, this time employing a measurement reference consisting of a substrate made from the same material and the same batch, which underwent the same cleaning processes. This excluded the possibility of any of these variables interfering with the measurement. This analysis was carried out using the Kasvi model K37-UVVIS instrument.

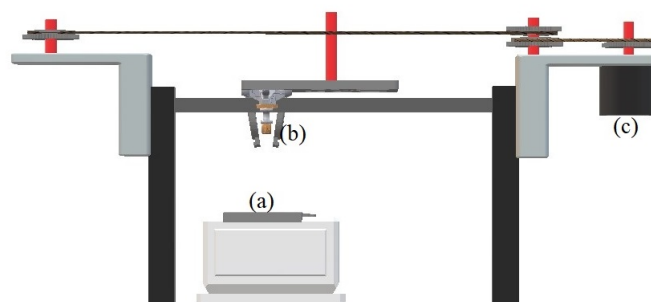


Figure 2 – (a) Glass substrate where the sol-gel solution is deposited. (b) A spray nozzle that disperses the coating fluid. (c) The Stepper motor was controlled by Arduino, where parameters such as speed, time between depositions, and amplitude of movement were controlled.

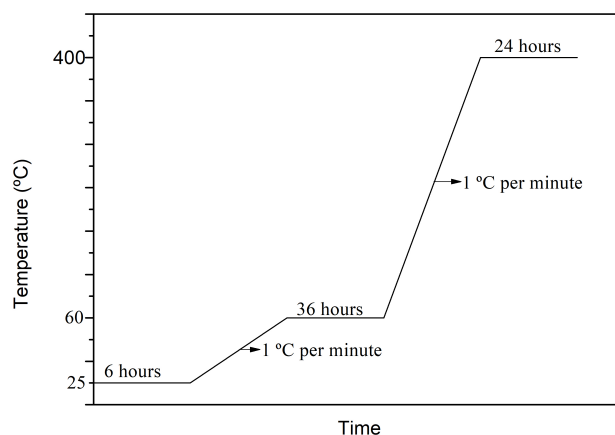


Figure 3 – Drying process representation in which the substrate with the coating fluid was subjected to obtain the  $\text{TiO}_2$  thin film.

In the study of the photocatalytic efficiency of  $\text{TiO}_2$  films, two solutions were prepared. One consisted of methylene blue, using laboratory-grade Proquímios powder with a molar mass of 373.90 g/mol, and the other contained methyl orange, utilizing laboratory-grade Dinâmica powder with a molar mass of 327.34 g/mol, at concentrations of  $1.34 \times 10^{-5}$  and  $1.28 \times 10^{-5}$  mol/L, respectively.

The initial solutions underwent a controlled dilution process to ensure result accuracy. Small quantities of distilled water were gradually added, aiming to achieve different concentrations of the dyes.

The  $\text{TiO}_2$  films used for the photocatalysis process were deposited using the spray coating method over the entire inner area of the beakers. This approach was employed to increase the contact area between the methylene blue solution and  $\text{TiO}_2$ , a strategy that optimized the efficiency of the photocatalysis process.

Before any contact between the  $\text{TiO}_2$  films and the methylene blue and methyl orange solutions, the optical characterization of the diluted solutions was performed. A UV-Vis spectrophotometer (Kasvi model K-37) was used to obtain absorbance curves for the solutions at various concentrations. These curves played a pivotal role in this research, serving as reference curves for later comparisons

with the photocatalysis results, as changes in absorbance were used as a basis for quantitative analysis.

After the UV-Vis characterization, the TiO<sub>2</sub> films were placed in contact with the initial methylene blue solution and kept in the dark for 1 hour, allowing for the establishment of adsorption-desorption equilibrium, as reported in previous studies [10, 33]. It's worth noting that any changes in the solution's concentration during this period, due to the absence of light, are related to adsorption and not photocatalysis.

Following the incubation period in the dark, a 15 W lamp emitting in the UVB and UVC spectral range was activated, marking a transition in the experiment where photocatalysis assumed a central role in modifying the solutions' concentrations. Subsequently, aliquots were collected at regular intervals, enabling the quantification of changes in solution concentration, the primary parameter used to determine the photocatalytic efficiency of the TiO<sub>2</sub> films.

### 3.3 Second Research

For the preparation of the coating fluid, the following products were used: Xylene from LabSynth, Titanium(IV) Butoxide with 98% purity, and Triton X-100 with 99.8% purity from Sigma-Aldrich, along with distilled water.

The procedure began with the addition of 0.026 mol of Xylene to  $6.60 \times 10^{-3}$  mol of Triton X-100, maintaining a precise proportion. This mixture was stirred for 30 minutes at 800 rpm at room temperature (25°C) using a magnetic stirrer. After this initial stirring period,  $1.47 \times 10^{-2}$  mol of Titanium(IV) Butoxide and 0.0167 mol of distilled water were added. The stirring was maintained for an additional 1 hour to ensure the homogeneity of the coating fluid.

A detailed cleaning procedure was applied to the borosilicate reactors used in this research. In the first stage of cleaning, an aqueous solution composed of 5% acetic acid, anionic surfactants, and coadjuvants was used in an ultrasonic bath for 1 hour. This initial procedure aimed to remove lipid residues and organic materials adhered to the surfaces of the reactors.

After this step, an ultrasonic bath containing exclusively distilled water was used twice to remove any residues from the solution used in the first step.

Following the completion of this stage, the ultrasonic bath was used for two additional cycles of 1 hour each, using acetone and isopropyl alcohol. This step aimed to eliminate polar substances and oils that may have persisted in the reactor.

With the reactors thoroughly cleaned, the process of film deposition begins. This process was carried out using a 0.4 mm diameter spray nozzle powered by an atmospheric air compressor with the airflow adjusted to  $0.002\text{ m}^3/\text{min}$ , dispersing the coating fluid throughout the reactor. Each reactor underwent a multilayer application process. In each application, 0.001g of coating fluid was deposited, and a 10-minute interval was observed between each layer, totaling 3 layers at the end of the process. This approach was adopted to prevent drips, especially due to the low viscosity of the coating fluid, thus ensuring the uniformity of the film in each applied layer.

Subsequently, the pre-calcination stage of the reactors begins. This process starts with a 2-hour pre-drying phase at room temperature ( $25^\circ\text{C}$ ), followed by a thermal treatment at  $60^\circ\text{C}$  for 24 hours. After this stage, the reactors were subjected to different calcination temperatures: 300, 400, 500, and  $600^\circ\text{C}$ . All reactors were exposed to a low temperature gradient of  $10^\circ\text{C}/\text{min}$ , promoting gradual evaporation of solvents, which helped to prevent cracks and fissures in the film.

The calcination temperatures were selected based on Thermogravimetric Analysis (TGA), as shown in Figure 4, which investigated the mass variation of  $\text{TiO}_2$  as a function of temperature. This analysis was performed using the Shimadzu TGA-50 equipment, in the range of 25 to  $1000^\circ\text{C}$ , with a gradient of  $10^\circ\text{C}/\text{min}$ , in a nitrogen atmosphere with an approximate flow of  $30\text{ mL}/\text{min}$ , as illustrated in Figure 4. The calcination process was limited to  $600^\circ\text{C}$  due to the softening point of the borosilicate substrate used for the construction of the reactors.

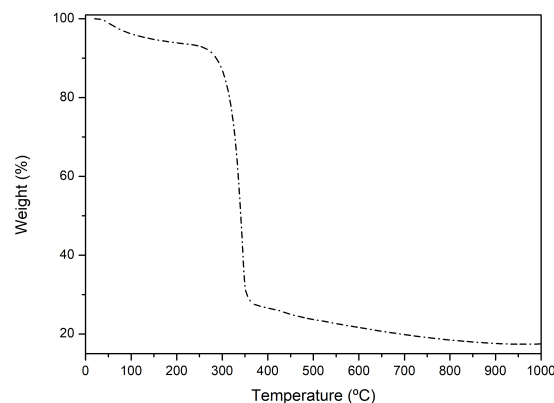


Figure 4 – Thermogravimetric analysis (TGA) of the coating fluid.

The samples were characterized using an Atomic Force Microscope (AFM) ASYLUM RESEARCH Cypher ES. X-ray diffraction (XRD) characterization was performed using the PANalytical X'Pert PRO model, emitting Cu-K $\alpha$  radiation, with a scan range of  $2\theta$  from  $20^\circ$  to  $80^\circ$ , a step size of  $0.02^\circ$  and a time per step of 2 seconds. Additionally, the samples were submitted to a FTIR characterization using a Perkin Elmer Spectrum 65 FTIR Spectrometer.

For the study of the photocatalytic efficiency of the reactors, a solution was prepared using 0.005 g of methylene blue powder from Proquímios laboratory, with a molar mass of 373.90 g/mol, diluted in 1 liter of distilled water, resulting in a solution with a concentration of  $1.34 \times 10^{-5}$  mol/L. This solution underwent a meticulous dilution process by adding controlled amounts of distilled water, resulting in different concentrations of methylene blue solutions.

These samples were subjected to absorbance measurements using the UV-Vis spectrophotometer from Kasvi, model K-37. This resulted in the respective absorbance curves for each concentration, as shown in Fig. 5 (a). With the acquisition of these curves, a linear fit was performed (Pearson's  $r=0.998$ ), from which the adjustment parameters were obtained, as depicted in Fig. 5 (b). These parameters enable the determination of the methylene blue solution concentration based on its absorbance after undergoing photocatalysis.

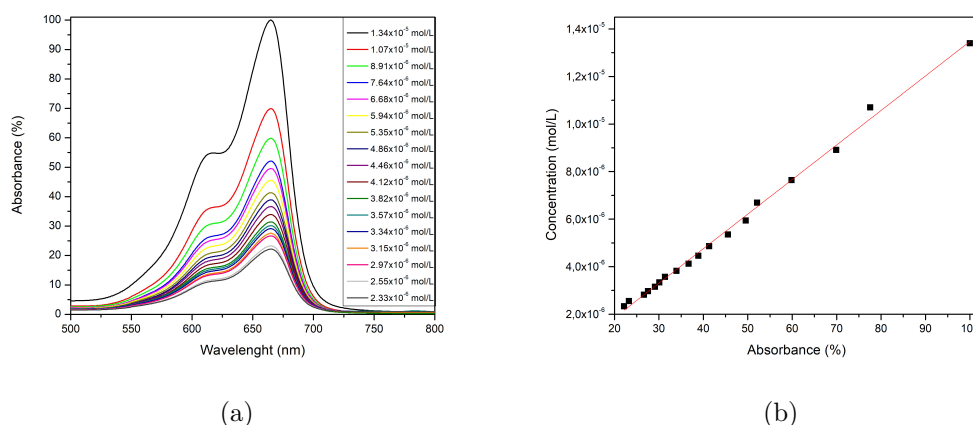


Figure 5 – (a) Reference curves obtained through controlled dilution of the initial methylene blue solution. (b) Linear fit for concentration determination, enabling the determination of these values from absorbance measurements.

The solutions were exposed to a 15W lamp with an emission spectrum as shown in Fig. 6. Aliquots were withdrawn at regular intervals, allowing quantification of changes in sample concentrations over the exposure time.

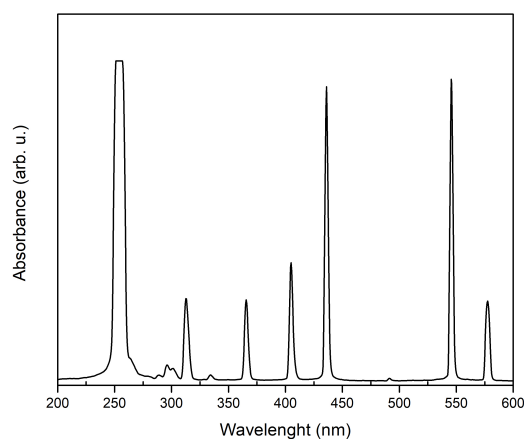


Figure 6 – The emission spectrum of the 15W lamp used for the photocatalysis procedure.

The reactor subjected to thermal treatment at 600 °C demonstrated the best photocatalytic efficiency. To obtain information on the reuse and degradation of this reactor, photocatalysis cycles were conducted. After a specific number of cycles, the reactor was left unused for one month before resuming the photocatalysis cycles. This procedure was adopted to investigate if the film self-degraded during the inactive period.

## 4 Results

### 4.1 First Research

The Scanning Electron Microscopy (SEM) technique was employed. In the powder material, aggregates of particles can be observed in Figure 7 (a), whereas in the film, it is no longer possible to observe these aggregates across their entire extent due to the uniformity enforced by the deposition machine.

When analyzing the deposited thin film using Energy-Dispersive X-ray Spectroscopy (EDS), it was possible to determine that the thin film exhibited a concentration of titanium and oxygen, as depicted in 7 (b) and 7 (c), respectively, thereby verifying and confirming the composition of the thin film. Furthermore, it was possible to determine the relative abundance of these chemical elements present in the film, where the concentration values of molar mass found were 58.80% for oxygen and 6.94% for titanium, as explicitly indicated in 7 (d).

It was also observed that at the edges of the substrate, there was the presence of cracks, likely caused by the greater accumulation of material at the substrate's ends. This accumulation is primarily associated with the effects of compressed air that sprays the solution. The material accumulation on the substrate, identified as the main factor in crack formation, was observed experimentally. In the initial experiments of this research, films with an excess of material exhibited a significant number of cracks, lacked mechanical strength, and displayed a fragmented microscopic morphology. These issues were only resolved through adjustments to the spray nozzle, resulting in a much thinner film.

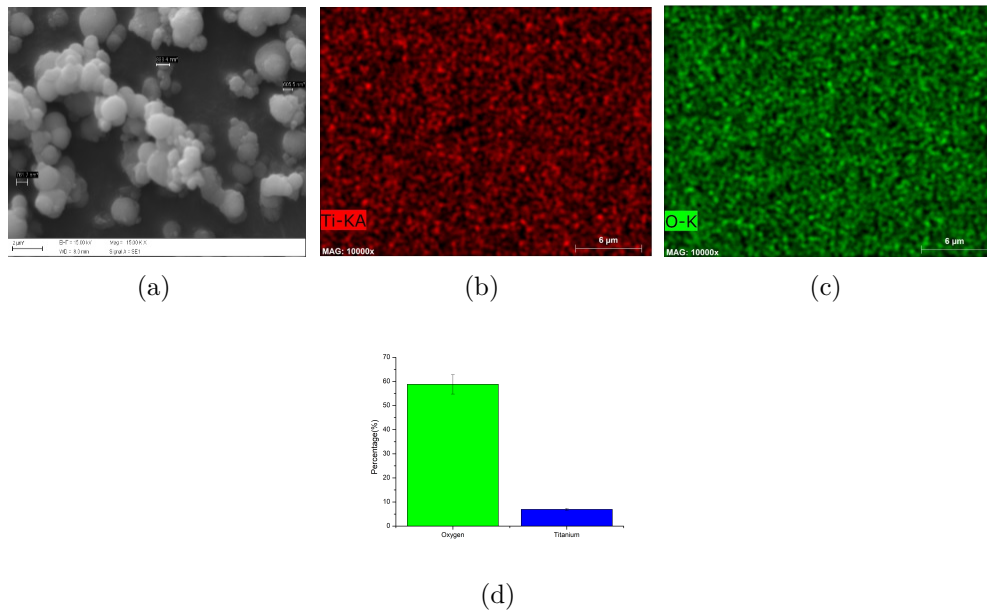


Figure 7 – (a) TiO<sub>2</sub> powder created through the identical calcination process as the thin film, employing the coating liquid. (b) Titanium mapping was conducted via Energy-dispersive X-ray spectroscopy. (c) Oxygen mapping was conducted via Energy-dispersive X-ray spectroscopy. (d) Titanium/oxygen concentration ratio in the thin film.

Through the use of Scanning Electron Microscopy (SEM), it became possible to conduct an analysis of the film's thickness based on the fragmentations found at the edges of the substrate, as shown in Figure 8 (a). With the assistance of the ImageJ software, thickness mapping was performed along 65 points of the film. These values were plotted and subsequently subjected to adjustment through normal distribution, enabling the determination of the mean film thickness value and its corresponding standard deviation of  $(741 \pm 42)$  nm.

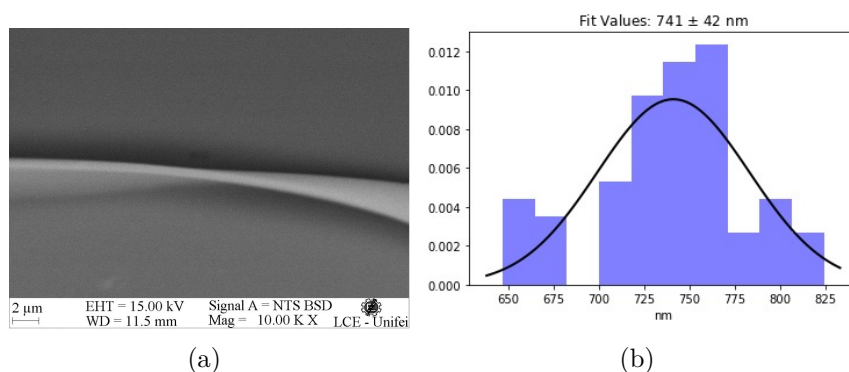


Figure 8 – (a) Image showing the fragmentation of the thin film where the thickness measurement was conducted. (b) Adjustment through a normal distribution, from which the value of the average film thickness along with its corresponding standard deviation was obtained.

The results of the analysis using Fourier Transform Infrared Spectroscopy (FTIR) confirm the previously discussed findings from the other characterization phases employed in this research effort. It is important to note that within the spectral range around  $1240\text{ cm}^{-1}$  and beyond, there is an observable absorption band in both cases. This presence is definitively attributed to the Ti—O—Ti linkage [34, 35].

Upon careful examination of the curve (a), oscillations are discernible and are associated with the substrate. The valley around  $1070\text{ cm}^{-1}$  can be linked to tri-, tetra-, penta-borate, and diborate groups, indicating the presence of  $BO_3$  and  $BO_4$  structures. This is also connected to the antisymmetric stretching of Si—O—Si bonds. Similarly, the peak at  $830\text{ cm}^{-1}$  corresponds to the symmetric stretching of the O—Si—O bond [36], as a result, all differences between the two curves are attributed to the presence of the substrate.

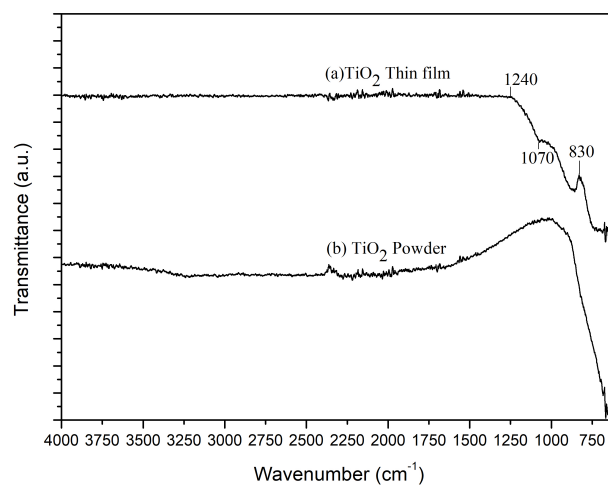


Figure 9 – Fourier-transform infrared spectroscopy spectra of: (a) TiO<sub>2</sub> thin film and (b) TiO<sub>2</sub> powder.

The analysis of compound absorbance through UV-Vis of a solution with powder form and a thin film tends to yield distinct results, influenced by phenomena such as surface effects, quantum confinement, reflections, and refractions, as well as film-specific characteristics like thickness, opacity, and molecular orientation, among others. As mentioned, numerous factors can contribute to the alteration of these characteristics [14-16]. In the case examined in this research, as depicted in Figure 10, the absorbance peak of the powder is shifted to shorter wavelengths compared to the absorbance peak of the thin film. This indicates that the film absorbs at lower energies, a desirable trait for its application in photovoltaic devices.

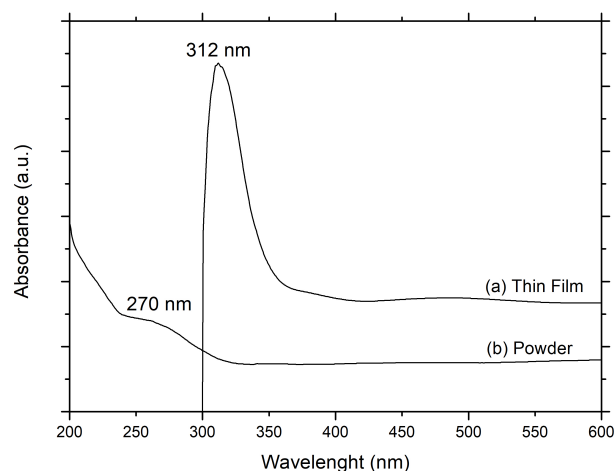


Figure 10 – UV-Vis Absorption Spectra: A comparison of absorbance spectra between the thin film (a) and powder diluted in distilled water (b). The changes in peak positions provide information about the optical properties.

In Figure 11, the X-ray Diffraction (XRD) results of the samples obtained after the calcination process are presented. Figure 11 (a) shows the XRD pattern of the particles obtained after the calcination at 400°C of the sol-gel solution by reverse micelles. The XRD pattern in Figure 11 (a) reveals peaks corresponding to the JCPDS 01-084-1285 standard, which is associated with the crystal structure of anatase [37, 38], being a remarkable result, as the anatase crystalline structure exhibits the highest photocatalytic activity [39, 40], demonstrating the effectiveness of the solution preparation and calcination processes.

Figure 11 (b) presents the XRD result of the thin film prepared from the same sol-gel solution and subjected to the same calcination process. In the XRD pattern of Figure 11 (b), peaks related to  $\text{TiO}_2$  in the anatase phase are also observed. Some peaks are not visible, and an amorphous region is detected due to the presence of the glass substrate. This outcome demonstrates that the use of low-cost spray coating equipment is promising, as even in the form of a thin film, the solution calcination resulted in a material with an anatase crystal structure. This characteristic is beneficial for applications in photovoltaic devices [41, 42],

photocatalysis [43, 44] and others.

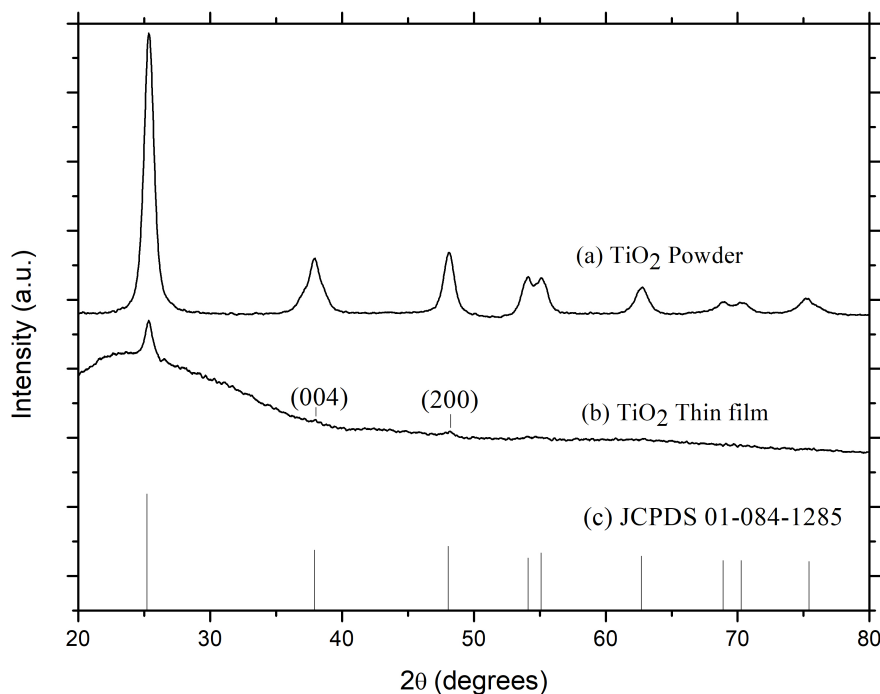


Figure 11 – (a) TiO<sub>2</sub> Nanopowder (b) TiO<sub>2</sub> Thin film and (c) Pattern JCPDS 01-084-1285 anatase TiO<sub>2</sub>. In (b) it is possible to observe the presence of peaks corresponding to the anatase structural pattern, as well as an amorphous region due to the presence of the glass substrate.

To verify the applicability of TiO<sub>2</sub> thin films produced by the deposition machine, thin films were synthesized in beakers, where methyl blue (MB) and methyl orange (MO) were chosen as model dyes for the study of the photocatalytic activity of these films. These dyes have characteristic peaks in the UV-Vis spectrum, which were identified through UV-Vis spectroscopy.

The absorbance curves that were obtained, provide a quantitative way to track the photodegradation of the samples, where higher absorbances represent higher concentrations of dyes in the solution. As the exposure time to ultraviolet light increases, there is a progressive decrease in the absorbance curves, as shown in Figure 20, indicating dye degradation due to photocatalysis. Due to the high

efficiency of degradation, the process can be visually and qualitatively affirmed, as shown in Figure 13. The images clearly demonstrate changes in dye concentrations in solutions, going from intense colors to considerably lighter tones.

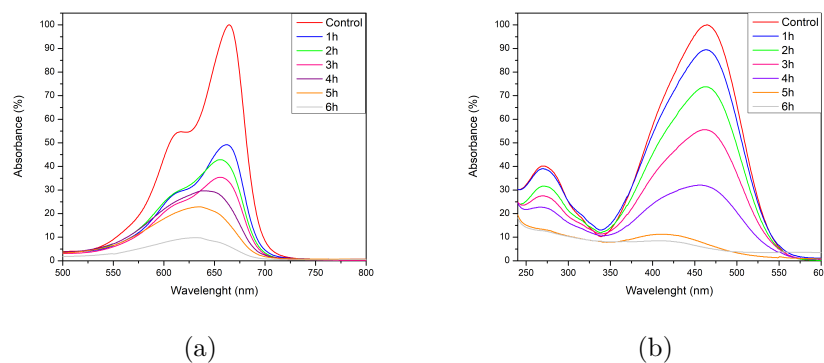


Figure 12 – Degradation process of methyl blue (a) and methyl orange (b) as a function of ultraviolet light exposure time.

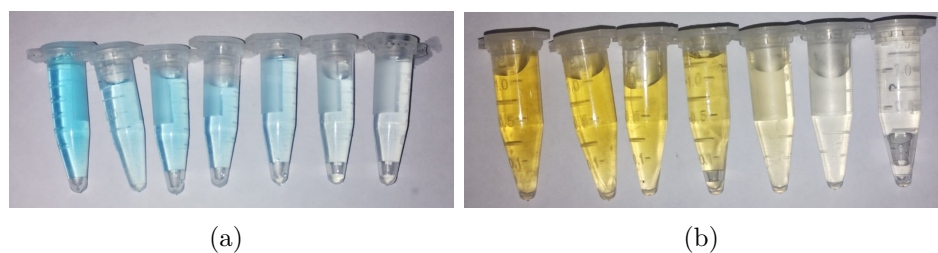


Figure 13 – Visual degradation process of methyl blue (a) and methyl orange (b).

One of the evaluated parameters was the degradation efficiency (DE), which was determined by analyzing the characteristic peaks of the dyes, given that the initial concentration ( $C_i$ ) of the sample is known, it is possible to obtain the concentration of the aliquot removed at a given time ( $C$ ) through comparisons of reference curves. Therefore, DE can be easily calculated using the equation [33, 45]

$$DE(\%) = \frac{C_i - C}{C_i} \times 100\% \quad (4.1)$$

The efficiency values are presented in Figure 14 (a), where curve (I) represents the photocatalysis of the aqueous dye solutions and curve (II) represents a measurement made to determine the self-degradation behavior of MB, where a value of less than 6% was found, which is negligible compared to the amount degraded by photocatalysis. For MO, it was not necessary to study its self-degradation behavior since this value is known and is close to 4% [46], which is also negligible when compared to the values of photocatalysis for this dye.

The kinetics of dye degradation, as shown in Figure 14 (b), was represented by a first-order reaction. The mathematical relationship that describes this kinetics is expressed as

$$\ln\left(\frac{C_i}{C}\right) = kt \quad (4.2)$$

Given that  $k$  is the rate constant ( $\text{min}^{-1}$ ) and  $t$  is the exposure time to UV light. To validate the model in question, linear adjustments were made to the experimentally obtained data for each of the dyes. The Pearson correlation coefficients ( $r$ ) found in these adjustments were equal to or greater than 0.95, providing values of  $k_{MB} = 0.0050 \text{ min}^{-1}$  e  $k_{MO} = 0.0047 \text{ min}^{-1}$ , which are consistent with values previously found in the literature [33].

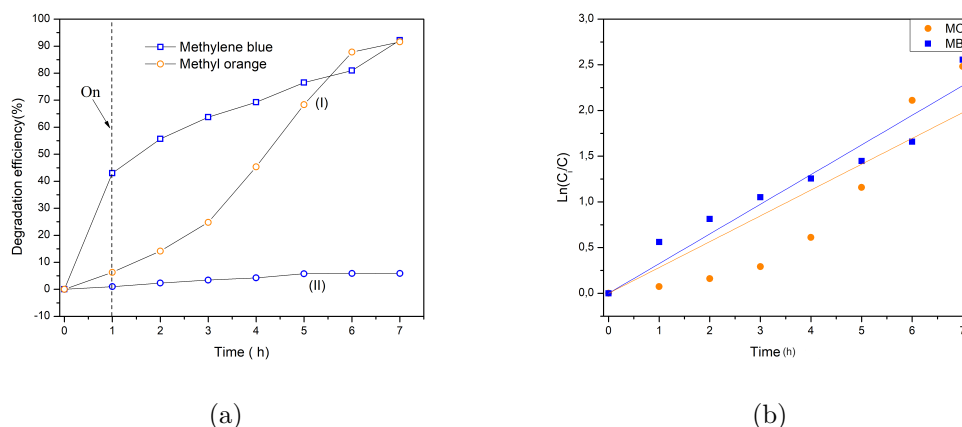


Figure 14 – (a) Efficiency of photodegradation of MB and MO with ultraviolet light irradiation on  $\text{TiO}_2$  films, where curve (I) represents photocatalysis and (II) Autodegradation of MB. (b) Kinetic data for the degradation of MB and MO.

An analysis of the contact angle between water and the  $\text{TiO}_2$  film was conducted with the aim of assessing surface wettability. The choice of water as the testing agent was due to the fact that the dye solutions used in the photodegradation process are aqueous. Angles close to  $180^\circ$  indicate entirely hydrophobic surfaces, whereas angles near  $0^\circ$  indicate completely hydrophilic surfaces; thus, the tendency for the liquid to spread across the surface increases as the contact angle decreases [47].

As illustrated in Figure 15, it can be observed that the measured contact angle was  $20.6^\circ$ . This value indicates excellent surface wettability, which highlights a strong interaction with water, facilitating the adsorption and diffusion of reactive species [48]. These characteristics play a fundamental role in the efficiency of photocatalytic reactions

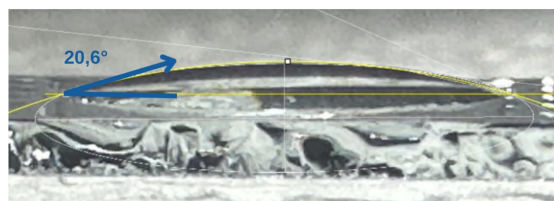


Figure 15 – Contact angle measurement evaluating the surface wettability of the  $\text{TiO}_2$  thin film in contact with water.

## 4.2 Second Research

Figure 16 presents the XRD results of  $\text{TiO}_2$  samples prepared via reverse micelle reaction [49, 50, 51] and subjected to different calcination temperatures (300, 400, 500 and 600 °C), aiming to investigate the effects of calcination temperature on the crystalline structure of  $\text{TiO}_2$  and its correlation with photocatalytic efficiency. The XRD results revealed that all samples predominantly exhibited the anatase phase of  $\text{TiO}_2$ , as visualized by the JCPDS 01-071-1166 pattern. However, there was variation in the intensity and quantity of crystalline peaks as the calcination temperature increased. The sample calcined at 300 °C showed only one diffraction peak at an angular position of 25.25°, indicating a relatively simple crystalline structure and possibly an initial formation phase. As the calcination temperature increased to 400 °C and 500 °C, the main peak at 25.25° was maintained, but higher intensity and additional peaks appeared, suggesting an increase in the crystallization of the anatase phase.

The results from Table 1 reveal that the crystallite size considerably increases with the rise in calcination temperature, ranging from 9.24 nm at 400 °C to 16.34 nm at 600 °C. At higher temperatures, the crystallinity increases, re-

sulting in narrower peaks (lower FWHM), this behavior indicates the growth of nanoparticle size [52]. Additionally, lattice strain diminishes with increasing calcination temperature, this pattern has been previously observed in the literature [53], suggesting a more uniform growth of the crystallites at elevated temperatures.

Although all samples exhibited the anatase phase, the sample calcined at 600 °C demonstrated a more defined structure, related to higher photocatalytic efficiency. However, factors beyond the crystalline structure, such as crystallite size, surface roughness, porosity, and specific surface area, may also influence the photocatalytic activity of TiO<sub>2</sub>. In summary, the XRD results indicate that the calcination temperature plays a crucial role in determining the crystalline structure of TiO<sub>2</sub>, which, in turn, can affect its photocatalytic properties. The correlation between the XRD results and the data from the table reinforces the importance of optimizing the calcination temperature to control the properties of TiO<sub>2</sub> and maximize its photocatalytic efficiency. However, further investigations are needed to fully understand the underlying mechanisms and optimize the photocatalytic performance of TiO<sub>2</sub> for practical applications.

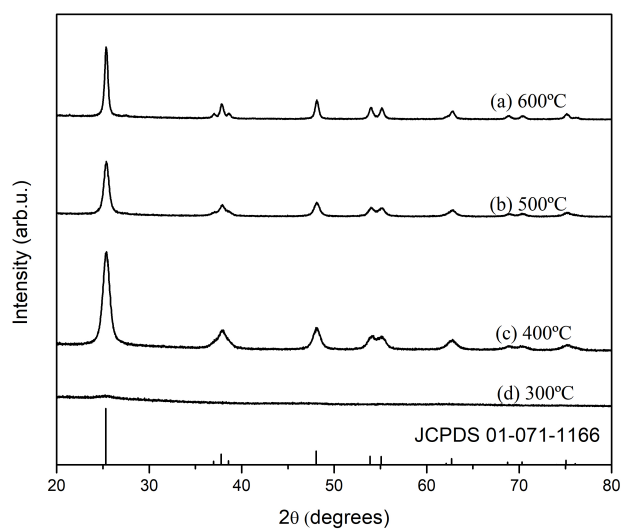


Figure 16 – Diffractogram for different calcination temperatures of TiO<sub>2</sub> thin films.

Table 1 – Effects of Calcination Temperature on Thin Film Properties

Temperature (°C)	Crystallite Size (nm)	Lattice Strain ( $\epsilon$ )	FWHM (°)
300	-	-	-
400	9.24	0.01792	4.00
500	13.28	0.01241	0.60
600	16.34	0.01010	0.40

Atomic Force Microscopy (AFM) is a useful technique for analyzing surface morphology, enabling the determination of surface roughness, which, among others parameters, is important for photocatalysis efficiency [54, 22]. Figures 17 and 18 show the TiO<sub>2</sub> films calcined at different temperatures. It is important to emphasize that all samples were analyzed in an area of 10x10 micrometers. However, the sample treated at 300 °C exhibited an atypical behavior compared to the other. An irregular and inconsistent film was observed in this sample. This behavior can be easily explained by considering the thermogravimetric analysis (TGA), as at 300 °C the film retained 87% of its total mass. It is evident that the non-uniformity of this film can be attributed to the incomplete degradation of the surfactant (Triton X-100). Thus, for the analysis of the roughness of this film, the area highlighted in Figure 17 (a) was considered. This area was chosen because it appeared visually more uniform.

The TiO<sub>2</sub> films calcined at 300, 400, 500, and 600°C exhibited root-mean-square roughness ( $\mathbf{R}_{RMS}$ ) values of 1.53, 1.99, 2.30, and 11.25 nm, respectively. These results are consistent with previous findings in the literature, which demonstrate that increasing surface roughness creates defects that introduce additional energy levels [55].

The energy levels created by the defects facilitate the transfer of electrons from the valence band ( $E_V$ ) to the defect levels ( $E_T$ ), and then to the conduction band ( $E_C$ ). This means that photons which previously did not have enough energy to excite the electron from the valence band to the conduction band can now do so, due to the existence of these new energy levels. This promotion of electrons to the conduction band increases the rate of production of hydroxyl radicals and superoxide, resulting in a higher degradation efficiency of the sample.

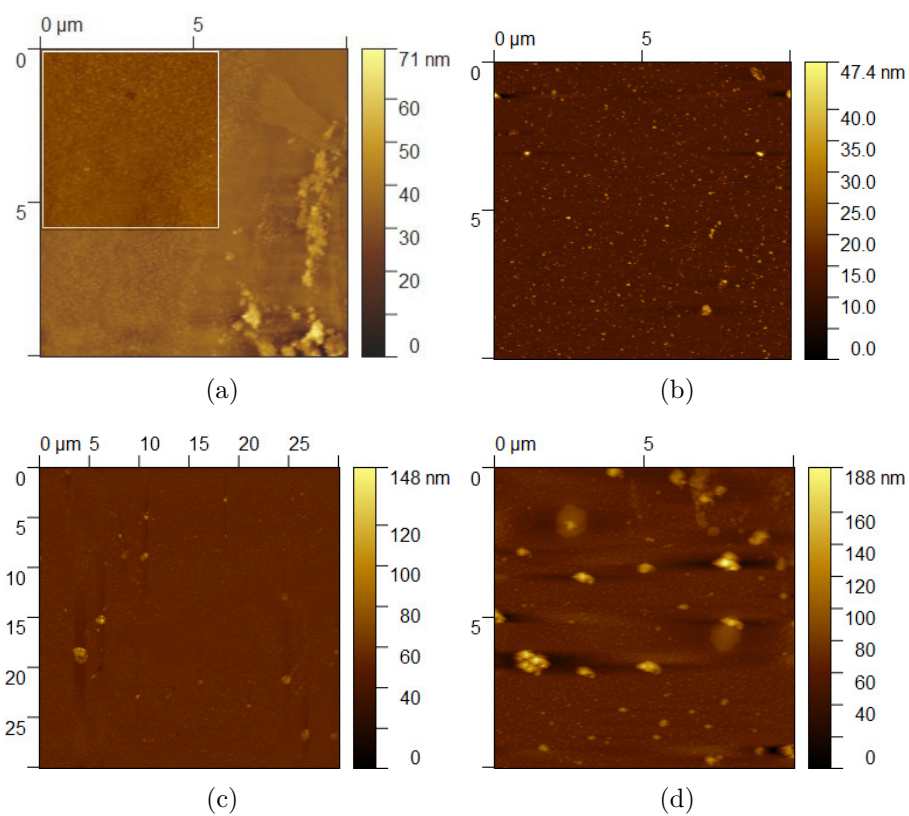


Figure 17 – AFM micrograph (2D) of the TiO<sub>2</sub> thin films with different calcination temperature, (a) 300 °C, (b) 400 °C, (c) 500 °C and (d) 600 °C.

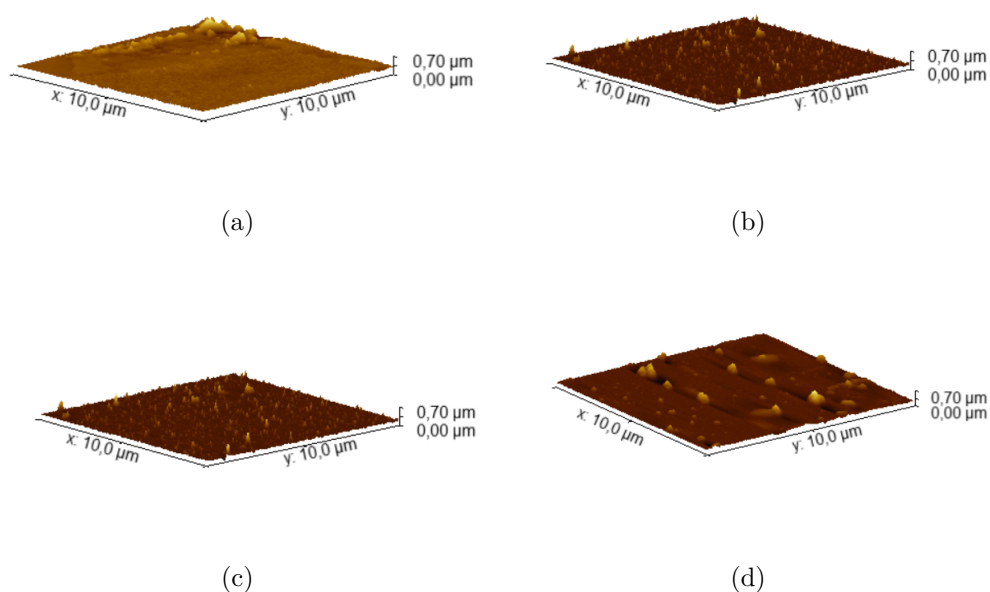


Figure 18 – AFM micrograph (3D) of the  $\text{TiO}_2$  thin films with different calcination temperature, (a) 300 °C, (b) 400 °C, (c) 500 °C and (d) 600 °C.

When combined the FTIR spectra of the materials used with the FTIR of  $\text{TiO}_2$  obtained after the calcination process, a clear decrease in the peaks located at approximately 3000, 1456, 1100, and 826  $\text{cm}^{-1}$  is observed, as represented in Figure 19 (a) and (b). These peaks are attributed to the asymmetric stretching of C-H bonds, deformation of the  $\text{CH}_3$  group, strong C-O-C band, and disubstituted benzene, respectively [56].

Starting at 400 °C, there is complete degradation of unwanted substances in the final composition of the thin film. At temperatures above this range, the only remaining evidence is that of Ti-O and O-H bonds, represented by the peaks at 1620 and 700  $\text{cm}^{-1}$ , respectively [57]. Despite limitations of the equipment, which cannot reach shorter wavelengths, it is still possible to observe the beginning of the characteristic peak of the Ti-O bond. Notably, the O-H bond, although still weakly observable in the 400 °C curve, disappears completely at higher temperatures. Therefore, the calcination process is crucial for resulting in a film composed almost exclusively of  $\text{TiO}_2$ .

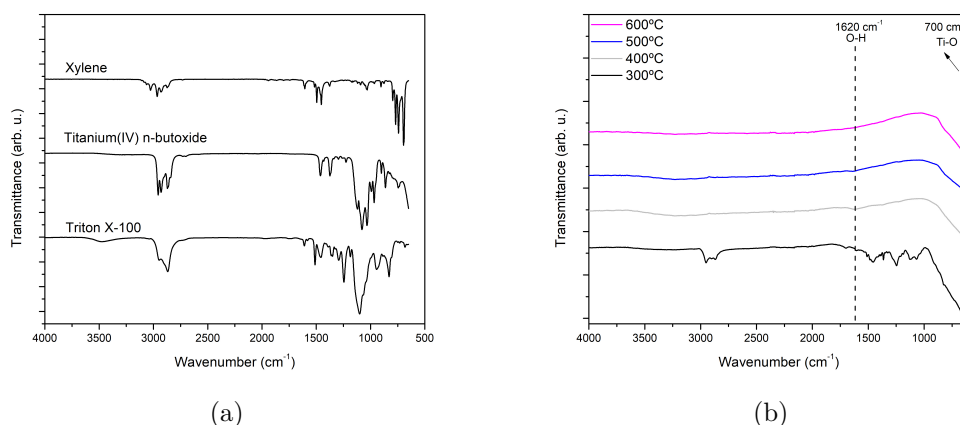


Figure 19 – The spectra obtained by FTIR analysis (a) show the characteristic absorption bands of the starting materials, while (b) highlights the formation of TiO<sub>2</sub>, despite the spectral range limitation.

Observing Figure 20, it is possible to see that the degradation of methylene blue became more intense with the increase in the calcination temperature of the reactors. As the temperature of the thermal treatment increases, there is an increase in the crystallite size accompanied by an increase in crystallinity. This higher crystallinity presents fewer defects on the surface and less particle aggregation, thus reducing the recombination of electron-hole pairs, which makes the photocatalysis process more efficient [58].

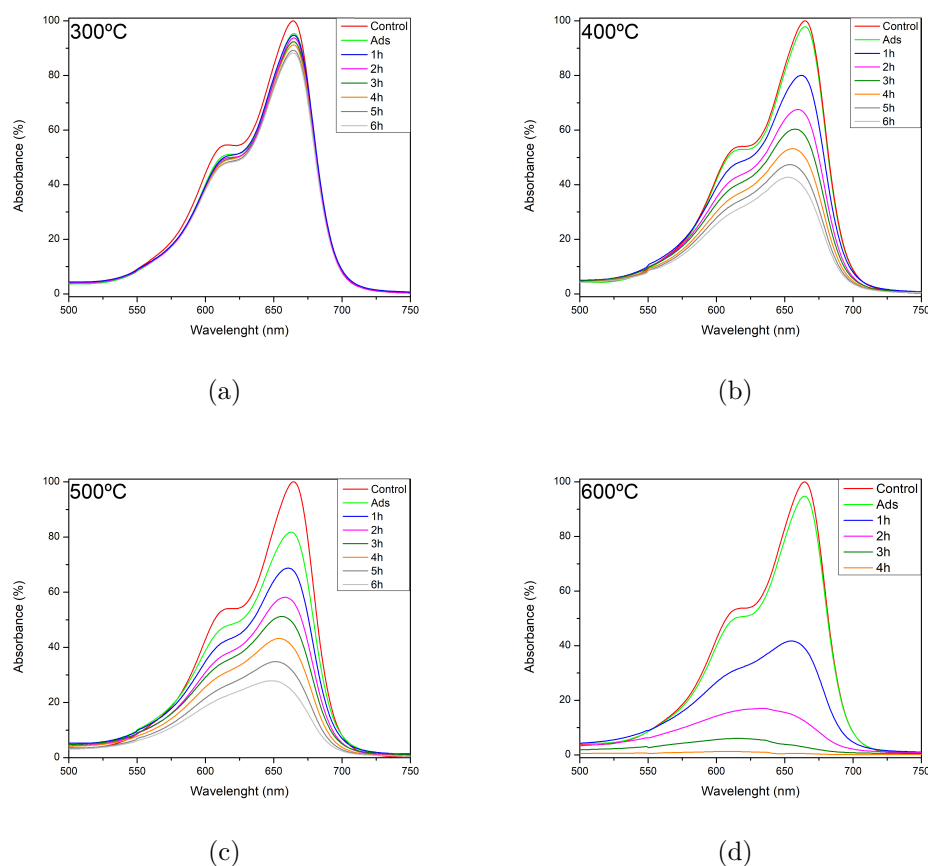


Figure 20 – Absorbance curves of the MB solution after the photocatalysis process using reactors calcined at different temperatures: (a) 300 °C, (b) 400 °C, (c) 500 °C, and (d) 600 °C.

The reactors subjected to calcination at 300, 400, 500, and 600 °C were exposed to a UV irradiation period of 6 hours. The reactor calcined at 600 °C achieved nearly complete degradation of methylene blue (MB) in just 4 hours of treatment, showing faster and more intense degradation compared to the other values.

With these absorbance curves and the linear fit of the reference curves, it was possible to quantitatively obtain the concentration of MB in the solution. Obtaining the concentrations made it possible to evaluate two parameters, degradation efficiency (DE), and degradation kinetics ( $k$ ) for all reactors.

Degradation efficiency is defined as the fraction of the contaminant that was removed from the solution during the degradation process, higher DE values indicate greater efficacy in the degradation process. Mathematically, DE is expressed as:

$$DE(\%) = \frac{C_i - C_t}{C_i} \times 100\% \quad (4.3)$$

Where:

- $C_i$  is the initial concentration of dye in the solution (in mol/L or g/L).
- $C_t$  is the concentration of contaminant in the solution at a given time  $t$  during the degradation process.

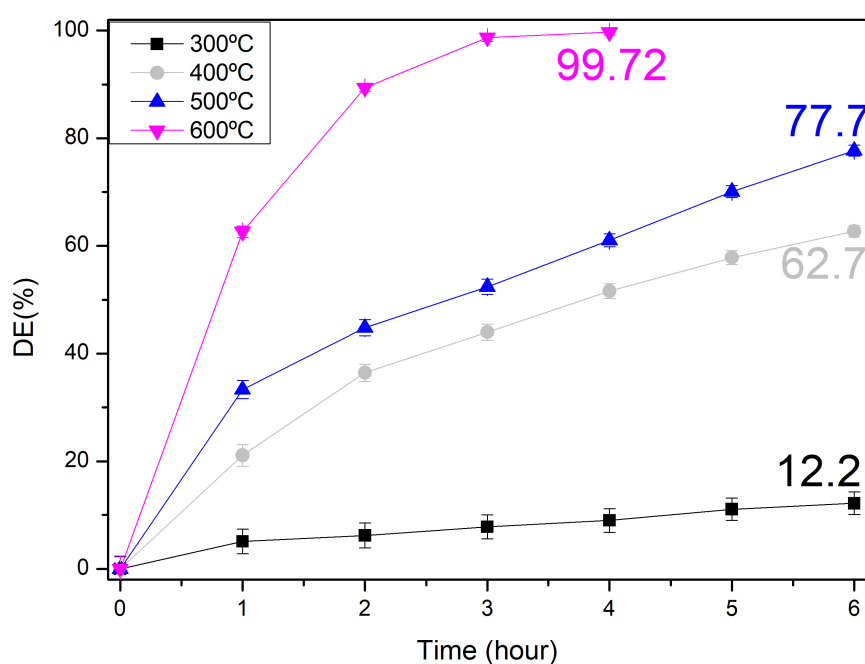


Figure 21 – Degradation efficiency (DE) obtained for reactors at different temperatures.

The degradation kinetics is also an important parameter for understanding how the degradation of the contaminant occurs throughout the degradation

process. In this case, the degradation kinetics is represented by the first-order mathematical model, given by:

$$\ln\left(\frac{C_0}{C_T}\right) = kt \quad (4.4)$$

Where:

- $k$  is the pseudo first-order rate constant expressed in  $\text{min}^{-1}$ .
- $t$  is the elapsed time since the beginning of the photocatalysis process.

When plotting Equation 4.4 as a function of time and performing a linear fit, the slope of the line will be the value of  $k$ , as depicted in Figure 22.

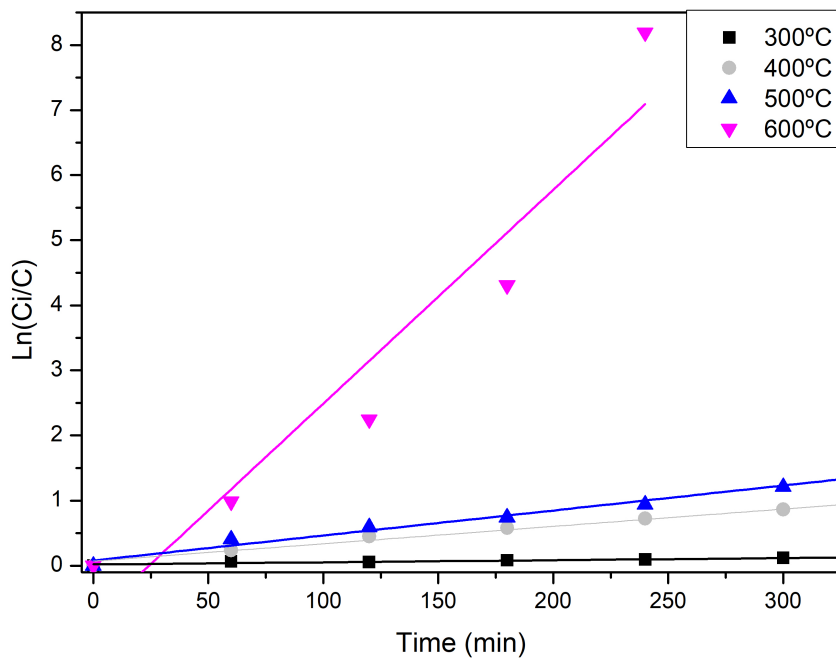


Figure 22 – Pseudo first-order rate constant ( $k$ ) obtained for reactors at different temperatures.

With this value, it becomes possible to understand the rate at which degradation is occurring; a higher value of  $k$  represents a faster degradation. The ob-

tained values are represented in Table 2. In our research, we have determined various rate constants ( $k$ ) for the photocatalytic degradation of pollutants using different calcination temperatures.

Table 2 – Values of the reaction kinetics for reactors calcined at different temperatures.

Temperature (°C)	$k$ (min <sup>-1</sup> )	Person's r
300	$3.21 \times 10^{-4} \pm 0.46 \times 10^{-4}$	0.95
400	$2.67 \times 10^{-3} \pm 0.15 \times 10^{-3}$	0.99
500	$3.84 \times 10^{-3} \pm 0.22 \times 10^{-3}$	0.99
600	$3.3 \times 10^{-2} \pm 0.56 \times 10^{-2}$	0.96

With the obtainment of both parameters, there is a comprehensive understanding of the overall efficiency of the degradation process accompanied by a detailed analysis of the reaction kinetics. These pieces of information make clear the superior performance of the reactor subjected to the 600 °C thermal treatment.

The degradation efficiency (DE) reached values close to 99.8%, demonstrating a high efficacy in the degradation process. Additionally, the degradation kinetics in this scenario were approximately 10 times higher than in the other reactors, indicating a significantly faster degradation rate.

To assess the stability of the TiO<sub>2</sub> film during the photocatalytic process, the sample was subjected to repeated experiments under identical conditions to evaluate its long-term stability. This evaluation is critical for determining the practical applicability of our photocatalytic films in environmental remediation. A total of ten cycles were performed, the first 5 cycles were consecutively tested, while the next 5 cycles were conducted after a month's interval. The purpose of this pause was to check if the photocatalyst present any kind of self-degradation or efficiency loss over prolonged inactivity.

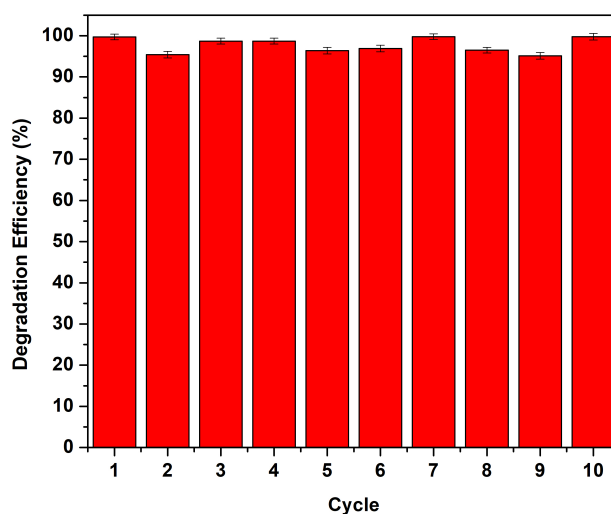


Figure 23 – Stability test of the photocatalyst over 10 degradation cycles.

The Figure 23 illustrates the stability test of the  $\text{TiO}_2$  film, where the catalyst presented a consistent performance across 10 consecutive degradation cycles. The material showed small changes in values, maintaining the degradation efficiency above 95% in every cycle, with an average degradation of  $97.69\% \pm 0.24\%$ . This result is satisfactory, considering the number of cycles and the one-month gap between the first five and the final five successive cycles.

These findings really support the fact that the photocatalyst is not only highly efficient but also resistant to factors that could compromise its long-term functionality. The one-month gap between the cycles was crucial for evaluating potential degradation due to exposure to environmental conditions while inactive. The results indicated that the material structure and active sites remained intact and fully functional. This suggests chemical and structural stability, confirming the usability of this material for extended periods without considerably losing its efficiency.

In practical terms, this means that the photocatalyst could be implemented in real-world applications where intermittent use or storage between periods of operation is common. It could maintain high degradation efficiency even after such

---

interruptions, further underlining its long-term sustainability for various applications. Overall, the tested photocatalyst showed itself to be a singularly robust material, able to provide consistent and reliable performance even under conditions that would usually degrade or diminish the effectiveness of the material.

## 5 Conclusion

In the present work, the successful realization of TiO<sub>2</sub> thin films synthesized with excellent adhesion was presented. The morphological analysis of these films under different calcination temperatures showed the improvement in the crystalline structure at higher calcination temperatures, which further improves photocatalytic activity showing a higher degradation efficiency and kinetics. Additionally, thermal treatment with higher temperatures, helped to remove impurities from the film, resulting in films consisting almost exclusively of TiO<sub>2</sub>.

Thin films has a major advantage over powders, because they eliminate filtration processes after photocatalysis. The spray coating route applied here is a useful method for large-area applications because of its ease and efficiency of depositing uniform thin films. The simplicity and efficiency of this method underlines its promise in large-scale applications.

Other exciting features involve possibilities for adaptation to different substrate sizes. The deposition system will be flexible enough to adapt to the specific needs of various applications, from small-sized substrates up to larger surfaces. This opens perspectives towards applications in environmental sectors, energy production, coatings, and sensors.

Coupling this efficient pollutant degradation with reusability and relatively easy synthesis, the TiO<sub>2</sub>-based thin films hold promise for a solution to eliminate such pollutants and reduce environmental problems. According to the above experimental results, the calcination temperature is critical for maximizing photocatalytic performance, and future research could explore the long-term stability and reusability of these films in various environmental conditions.

# Bibliography

- 1 OMER, A. M. Energy, environment and sustainable development. *Renewable and sustainable energy reviews*, Elsevier, v. 12, n. 9, p. 2265–2300, 2008. [15](#)
- 2 PARRINO, F.; PALMISANO, L. *Titanium Dioxide (TiO<sub>2</sub>) and Its Applications*. [S.l.]: elsevier, 2020. [15](#)
- 3 NEGISHI, N.; TAKEUCHI, K.; IBUSUKI, T. Surface structure of the tio<sub>2</sub> thin film photocatalyst. *Journal of materials science*, Springer, v. 33, n. 24, p. 5789–5794, 1998. [15](#)
- 4 HUANG, C.-W. et al. Hydrogen generation from photocatalytic water splitting over tio<sub>2</sub> thin film prepared by electron beam-induced deposition. *international journal of hydrogen energy*, Elsevier, v. 35, n. 21, p. 12005–12010, 2010. [15](#)
- 5 LIU, J. et al. Photovoltaic performance improvement of dye-sensitized solar cells based on tantalum-doped tio<sub>2</sub> thin films. *Electrochimica Acta*, Elsevier, v. 56, n. 1, p. 396–400, 2010. [15](#)
- 6 YAO, K. et al. Comparison of photocatalytic activities of various dye-modified tio<sub>2</sub> thin films under visible light. *Surface and Coatings Technology*, Elsevier, v. 203, n. 5-7, p. 922–924, 2008. [15](#)
- 7 JUNG, C.-K. et al. Plasma surface modification of tio<sub>2</sub> photocatalysts for improvement of catalytic efficiency. *Surface and Coatings Technology*, Elsevier, v. 200, n. 5-6, p. 1320–1324, 2005. [15](#)
- 8 EUFINGER, K. et al. Tio<sub>2</sub> thin films for photocatalytic applications. *Thin solid films: process and applications*, v. 37661, p. 2, 2008. [15](#)
- 9 XU, C.; RANGAIAH, G.; ZHAO, X. Photocatalytic degradation of methylene blue by titanium dioxide: experimental and modeling study. *Industrial & Engineering Chemistry Research*, ACS Publications, v. 53, n. 38, p. 14641–14649, 2014. [15](#)
- 10 DIN, M. I. et al. Fundamentals and photocatalysis of methylene blue dye using various nanocatalytic assemblies—a critical review. *Journal of Cleaner Production*, Elsevier, v. 298, p. 126567, 2021. [15](#), [22](#)
- 11 CHEN, D. et al. Photocatalytic degradation of organic pollutants using tio<sub>2</sub>-based photocatalysts: A review. *Journal of Cleaner Production*, Elsevier, v. 268, p. 121725, 2020. [15](#)

- 12 KIM, B. et al. Bactericidal effect of tio2 photocatalyst on selected food-borne pathogenic bacteria. *Chemosphere*, Elsevier, v. 52, n. 1, p. 277–281, 2003. 15
- 13 DHOLAM, R. et al. Physically and chemically synthesized tio2 composite thin films for hydrogen production by photocatalytic water splitting. *International journal of hydrogen energy*, Elsevier, v. 33, n. 23, p. 6896–6903, 2008. 15
- 14 ENYOH, C. E. et al. An overview of emerging pollutants in air: Method of analysis and potential public health concern from human environmental exposure. *Trends in environmental analytical chemistry*, Elsevier, v. 28, p. e00107, 2020. 15
- 15 BINAS, V. et al. Modified tio 2 based photocatalysts for improved air and health quality. *Journal of Materiomics*, Elsevier BV, v. 3, n. 1, p. 3–16, mar. 2017. ISSN 2352-8478. Disponível em: <<http://dx.doi.org/10.1016/j.jmat.2016.11.002>>. 15
- 16 KHAN, S. et al. Emerging contaminants of high concern for the environment: Current trends and future research. *Environmental Research*, Elsevier, v. 207, p. 112609, 2022. 15
- 17 LEI, M. et al. Overview of emerging contaminants and associated human health effects. *BioMed research international*, Hindawi, v. 2015, 2015. 15
- 18 FENG, G.; HUANG, H.; CHEN, Y. Effects of emerging pollutants on the occurrence and transfer of antibiotic resistance genes: A review. *Journal of Hazardous Materials*, Elsevier, v. 420, p. 126602, 2021. 15
- 19 SAYEGH, S. et al. N-doped tio2 nanotubes synthesized by atomic layer deposition for acetaminophen degradation. *Colloids and Surfaces A: Physicochemical and Engineering Aspects*, Elsevier, v. 655, p. 130213, 2022. 15
- 20 RAJ, I. L. P. et al. Study on the synergistic effect of terbium-doped sno 2 thin film photocatalysts for dye degradation. *Journal of Nanoparticle Research*, Springer, v. 22, p. 1–14, 2020. 15
- 21 PINTON, J. H. B. et al. Development of an automated and cost-effective apparatus for sol-gel solution deposition using spray coating technique and its application for tio2-based photocatalytic films. *Materials Chemistry and Physics*, Elsevier, v. 318, p. 129213, 2024. 15
- 22 VADIVEL, S.; RAJARAJAN, G. Effect of mg doping on structural, optical and photocatalytic activity of sno 2 nanostructure thin films. *Journal of Materials Science: Materials in Electronics*, Springer, v. 26, p. 3155–3162, 2015. 15, 38

- 23 KUMAR, M. et al. Biosynthesis of tin oxide nanoparticles using psidium guajava leave extract for photocatalytic dye degradation under sunlight. *Materials Letters*, Elsevier, v. 215, p. 121–124, 2018. 15
- 24 DAS, O. et al. Highly active carbon supported sn/sno2 photocatalysts for degrading organic dyes. In: IOP PUBLISHING. *Journal of Physics: Conference Series*. [S.l.], 2018. v. 1086, n. 1, p. 012011. 15
- 25 RADECKA, M. et al. Tio2/sno2 nanotubes for hydrogen generation by photoelectrochemical water splitting. *International Journal of Hydrogen Energy*, Elsevier, v. 40, n. 1, p. 841–851, 2015. 15
- 26 SHWETHARANI, R. et al. Photocatalytic semiconductor thin films for hydrogen production and environmental applications. *International Journal of Hydrogen Energy*, Elsevier BV, v. 45, n. 36, p. 18289–18308, jul. 2020. ISSN 0360-3199. Disponível em: <<http://dx.doi.org/10.1016/j.ijhydene.2019.03.149>>. 15
- 27 WU, X. et al. Preparation of bi-based photocatalysts in the form of powdered particles and thin films: a review. *Journal of Materials Chemistry A*, Royal Society of Chemistry (RSC), v. 8, n. 31, p. 15302–15318, 2020. ISSN 2050-7496. Disponível em: <<http://dx.doi.org/10.1039/D0TA01180K>>. 15
- 28 RYU, J. et al. Photocatalytic tio2 thin films by aerosol-deposition: From micron-sized particles to nano-grained thin film at room temperature. *Applied Catalysis B: Environmental*, Elsevier BV, v. 83, n. 1–2, p. 1–7, set. 2008. ISSN 0926-3373. Disponível em: <<http://dx.doi.org/10.1016/j.apcatb.2008.01.020>>. 15
- 29 PEDANEKAR, R.; SHAIKH, S.; RAJPURE, K. Thin film photocatalysis for environmental remediation: A status review. *Current Applied Physics*, Elsevier BV, v. 20, n. 8, p. 931–952, ago. 2020. ISSN 1567-1739. Disponível em: <<http://dx.doi.org/10.1016/j.cap.2020.04.006>>. 15
- 30 BHATKHANDI, D. S.; PANGARKAR, V. G.; BEENACKERS, A. A. C. M. Photocatalytic degradation for environmental applications—a review. *Journal of Chemical Technology & Biotechnology: International Research in Process, Environmental & Clean Technology*, Wiley Online Library, v. 77, n. 1, p. 102–116, 2002. 17
- 31 NASCIMENTO, J. L. A. do et al. The influence of synthesis methods and experimental conditions on the photocatalytic properties of sno2: a review. *Catalysts*, MDPI, v. 12, n. 4, p. 428, 2022. 17
- 32 AL-YASERI, A. et al. Effects of cleaning process using toluene and acetone on water-wet-quartz/co2 and oil-wet-quartz/co2 wettability. *Journal of Petroleum Science and Engineering*, Elsevier, v. 208, p. 109555, 2022. 18

- 33 SINGH, R.; DUTTA, S. Synthesis and characterization of solar photoactive tio<sub>2</sub> nanoparticles with enhanced structural and optical properties. *Advanced Powder Technology*, Elsevier, v. 29, n. 2, p. 211–219, 2018. [22](#), [33](#), [34](#)
- 34 LI, W. et al. Using 3-isocyanatopropyltrimethoxysilane to decorate graphene oxide with nano-titanium dioxide for enhancing the anti-corrosion properties of epoxy coating. *Polymers*, MDPI, v. 12, n. 4, p. 837, 2020. [29](#)
- 35 ZEWEDE, B.; PITLIYA, P.; RAGHAVAN, D. The role of surface modified tio<sub>2</sub> nanoparticles on the mechanical and thermal properties of ctbn toughened epoxy nanocomposite. *Journal of Materials Science*, Springer, v. 51, p. 9314–9329, 2016. [29](#)
- 36 SHAO, G. et al. Thermal shock behavior and infrared radiation property of integrative insulations consisting of mosi<sub>2</sub>/borosilicate glass coating and fibrous zro<sub>2</sub> ceramic substrate. *Surface and Coatings Technology*, Elsevier, v. 270, p. 154–163, 2015. [29](#)
- 37 THAMAPHAT, K.; LIMSUWAN, P.; NGOTAWORNCHAI, B. Phase characterization of tio<sub>2</sub> powder by xrd and tem. *Agriculture and Natural Resources*, v. 42, n. 5, p. 357–361, 2008. [31](#)
- 38 SANKAPAL, B.; LUX-STEINER, M. C.; ENNAOUI, A. Synthesis and characterization of anatase-tio<sub>2</sub> thin films. *Applied surface science*, Elsevier, v. 239, n. 2, p. 165–170, 2005. [31](#)
- 39 ZHANG, J. et al. New understanding of the difference of photocatalytic activity among anatase, rutile and brookite tio<sub>2</sub>. *Physical Chemistry Chemical Physics*, The Royal Society of Chemistry, v. 16, n. 38, p. 20382–20386, 2014. [31](#)
- 40 TANG, H. et al. Electrical and optical properties of tio<sub>2</sub> anatase thin films. *Journal of applied physics*, American Institute of Physics, v. 75, n. 4, p. 2042–2047, 1994. [31](#)
- 41 WENG, K.-W.; HUANG, Y.-P. Preparation of tio<sub>2</sub> thin films on glass surfaces with self-cleaning characteristics for solar concentrators. *Surface and Coatings Technology*, Elsevier, v. 231, p. 201–204, 2013. [31](#)
- 42 SAWICKA-CHUDY, P. et al. Review of the development of copper oxides with titanium dioxide thin-film solar cells. *AIP Advances*, AIP Publishing, v. 10, n. 1, 2020. [31](#)
- 43 JUNG, C.-K. et al. Synthesis of tio<sub>2</sub> photocatalyst and study on their improvement technology of photocatalytic activity. *Surface and Coatings Technology*, Elsevier, v. 200, n. 1-4, p. 534–538, 2005. [32](#)

- 44 ARCONADA, N. et al. Synthesis and photocatalytic properties of dense and porous tio<sub>2</sub>-anatase thin films prepared by sol-gel. *Applied Catalysis B: Environmental*, Elsevier, v. 86, n. 1-2, p. 1-7, 2009. [32](#)
- 45 YANG, H. et al. Sol-gel synthesis of tio<sub>2</sub> nanoparticles and photocatalytic degradation of methyl orange in aqueous tio<sub>2</sub> suspensions. *Journal of Alloys and Compounds*, Elsevier, v. 413, n. 1-2, p. 302-306, 2006. [33](#)
- 46 LI, Y. et al. Photocatalytic degradation of methyl orange by tio<sub>2</sub>-coated activated carbon and kinetic study. *Water research*, Elsevier, v. 40, n. 6, p. 1119-1126, 2006. [34](#)
- 47 ZISMAN, W. A. Relation of the equilibrium contact angle to liquid and solid constitution. In: . [S.l.]: ACS Publications, 1964. [35](#)
- 48 YANG, X. et al. Fabrication of porous hydrophilic cn/pani heterojunction film for high-efficiency photocatalytic h<sub>2</sub> evolution. *Catalysts*, MDPI, v. 13, n. 1, p. 139, 2023. [35](#)
- 49 GHIACI, M.; AGHAEI, H.; ABBASPUR, A. Size-controlled synthesis of zro<sub>2</sub>-tio<sub>2</sub> nanoparticles prepared via reverse micelle method: investigation of particle size effect on the catalytic performance in vapor phase beckmann rearrangement. *Materials Research Bulletin*, Elsevier, v. 43, n. 5, p. 1255-1262, 2008. [36](#)
- 50 HSU, C.-Y. et al. Nano titanium oxide (nano-tio<sub>2</sub>): A review of synthesis methods, properties, and applications. *Case Studies in Chemical and Environmental Engineering*, Elsevier, p. 100626, 2024. [36](#)
- 51 OLIVEIRA, A. et al. Preparation and characterization of palladium-doped titanium dioxide for solar cell applications. *Materials Science and Engineering: B*, Elsevier, v. 280, p. 115702, 2022. [36](#)
- 52 ORENDORZ, A. et al. Phase transformation and particle growth in nanocrystalline anatase tio<sub>2</sub> films analyzed by x-ray diffraction and raman spectroscopy. *Surface Science*, Elsevier, v. 601, n. 18, p. 4390-4394, 2007. [37](#)
- 53 GORSKA, P. et al. Tio<sub>2</sub> photoactivity in vis and uv light: The influence of calcination temperature and surface properties. *Applied Catalysis B: Environmental*, Elsevier, v. 84, n. 3-4, p. 440-447, 2008. [37](#)
- 54 HAYA, S. et al. Sol-gel synthesis of sr-doped sno<sub>2</sub> thin films and their photocatalytic properties. *Materials Research Express*, IOP Publishing, v. 4, n. 10, p. 106406, 2017. [38](#)

55 HOSSEINI, Z. S. et al. Enhanced visible photocatalytic performance of undoped tio<sub>2</sub> nanoparticles thin films through modifying the substrate surface roughness. *Materials Chemistry and Physics*, Elsevier, v. 279, p. 125530, 2022. [38](#)

56 HTWE, Y.; ABDULLAH, M.; MARIATTI, M. Optimization of graphene conductive ink using solvent exchange techniques for flexible electronics applications. *Synthetic Metals*, Elsevier, v. 274, p. 116719, 2021. [40](#)

57 AL-AMIN, M. et al. Solar assisted photocatalytic degradation of reactive azo dyes in presence of anatase titanium dioxide. *Int. J. Latest Res. Eng. Technol*, v. 2, n. 3, p. 14–21, 2016. [40](#)

58 ABDELKADER, E. et al. SnO<sub>2</sub> foam grain-shaped nanoparticles: Synthesis, characterization and uva light induced photocatalysis. *Journal of Alloys and Compounds*, Elsevier, v. 679, p. 408–419, 2016. [41](#)